

# Plasma-Driven Synthesis of Self-Supported Nickel-Iron Nanostructures for Water Electrolysis

**Citation for published version (APA):**

Ranade, A., Lao, M., Timmer, R. H. M., Zoethout, E., van Eck, H. J. N., & Tsampas, M. N. (2023). Plasma-Driven Synthesis of Self-Supported Nickel-Iron Nanostructures for Water Electrolysis. *Advanced Materials Interfaces*, 10(34), Article 2300486. <https://doi.org/10.1002/admi.202300486>

**Document license:**  
CC BY

**DOI:**  
[10.1002/admi.202300486](https://doi.org/10.1002/admi.202300486)

**Document status and date:**  
Published: 04/12/2023

**Document Version:**  
Publisher's PDF, also known as Version of Record (includes final page, issue and volume numbers)

**Please check the document version of this publication:**

- A submitted manuscript is the version of the article upon submission and before peer-review. There can be important differences between the submitted version and the official published version of record. People interested in the research are advised to contact the author for the final version of the publication, or visit the DOI to the publisher's website.
- The final author version and the galley proof are versions of the publication after peer review.
- The final published version features the final layout of the paper including the volume, issue and page numbers.

[Link to publication](#)

**General rights**

Copyright and moral rights for the publications made accessible in the public portal are retained by the authors and/or other copyright owners and it is a condition of accessing publications that users recognise and abide by the legal requirements associated with these rights.

- Users may download and print one copy of any publication from the public portal for the purpose of private study or research.
- You may not further distribute the material or use it for any profit-making activity or commercial gain
- You may freely distribute the URL identifying the publication in the public portal.

If the publication is distributed under the terms of Article 25fa of the Dutch Copyright Act, indicated by the "Taverne" license above, please follow below link for the End User Agreement:

[www.tue.nl/taverne](http://www.tue.nl/taverne)

**Take down policy**

If you believe that this document breaches copyright please contact us at:

[openaccess@tue.nl](mailto:openaccess@tue.nl)

providing details and we will investigate your claim.

# Plasma-Driven Synthesis of Self-Supported Nickel-Iron Nanostructures for Water Electrolysis

Ameya Ranade, Mengmeng Lao, Remco H.M. Timmer, Erwin Zoethout, Hans J.N. van Eck, and Mihalis N. Tsampas\*

Nickel-based electrocatalysts are deemed as promising low-cost, earth-abundant materials in the development of the next-generation alkaline and anion exchange membrane water electrolyzers. Herein, a plasma-processing technique is presented for fabricating self-supported nanostructures from planar NiFe substrates and its performance for water splitting reactions. Irradiating the samples with helium plasma results in the formation of nano-tendrils, which are affixed to the metallic substrate. This unique design not only enhances charge and mass transport, but also increases the electrochemical surface area by 3 to 4 times, as compared to the unmodified/planar surfaces. For the benchmark  $10 \text{ mAcm}^{-2}_{\text{geo}}$  current density, the nanostructured electrodes demonstrate overpotentials of 330 and 354 mV for oxygen evolution reaction and hydrogen evolution reaction respectively in 1 M-KOH. Moving forward, application of this technique can be extended for fabricating self-supported 3D substrates (e.g., foams, felts, perforated sheets), all of which find practical applications in energy conversion and storage devices.

## 1. Introduction

Hydrogen is considered as a future energy carrier, which is conventionally produced via fossil fuel-intensive processes, resulting in greenhouse gas emissions. Water electrolysis, when coupled with renewable energy sources is a promising approach for producing green hydrogen, due to its eco-friendliness and


ability to obtain high hydrogen purity. In the development of water electrolyzers, platinum (Pt) for hydrogen evolution reaction (HER), and the oxides of ruthenium and iridium (Ir) for oxygen evolution reaction (OER) are considered as the benchmark catalysts.<sup>[1]</sup> However, their high cost and scarcity has limited the scaling up of water electrolysis on a global level. Hence, recent efforts have been devoted for developing low-cost, earth-abundant electrocatalysts.<sup>[2–8]</sup> Amongst the alternatives, nickel (Ni) is a well-known material and has been extensively studied for water electrolysis in alkaline media.<sup>[9–12]</sup> Particularly, nickel-iron compounds are considered as promising materials due to the synergistic effects between nickel and iron. On the anodic side, low levels of iron (Fe) incorporation from the electrolyte into the nickel electrode has a significant

increase in the catalyst performance for OER.<sup>[13,14]</sup> As cathodes, nickel-iron (NiFe) compounds can mitigate hydride formation during HER on the electrode surface, which is known to cause severe degradation in the case of monometallic nickel, and thus help to restore the electrode performance.<sup>[15,16]</sup> Thus, NiFe compounds have also been employed as bifunctional catalysts for electrochemical water splitting, owing to their increased activity.<sup>[17–22]</sup>

In addition to increasing the catalyst's activity (by efficient catalyst design), increasing the number of active sites via nanostructuring or interfacial engineering is often employed to improve the catalyst performance.<sup>[23]</sup> Nanostructured catalysts (that are typically synthesized in a top-down or a bottom-up manner<sup>[24]</sup>) possess several advantages such as providing different transition states, lowering the activation energy, increasing the number of active sites that ultimately alleviate overpotentials and minimize energy losses.<sup>[25]</sup> In the literature, a variety of methods for synthesizing nickel-based nanostructures have been reported.<sup>[26–32]</sup> The nanostructured electrocatalysts are typically synthesized in a powder form and thus, require a binder to coat them on a substrate.<sup>[33]</sup> The extra interfaces between the catalyst, substrate and the electrolyte can cause charge and mass transfer limitations as well as restrict the availability of active sites.<sup>[33]</sup> Carbon-based additives and/or supports can help to improve charge transfer limitations. However, they can corrode under OER conditions leading to mechanical shedding, and weakening of

A. Ranade, M. Lao, R. H.M. Timmer, E. Zoethout, H. J.N. van Eck, M. N. Tsampas, A. Ranade, M. Lao, R. H. Timmer, E. Zoethout, H. J. van Eck, M. N. Tsampas  
 Dutch Institute for Fundamental Energy Research (DIFFER)  
 De Zaale 20, Eindhoven 5612 AJ, The Netherlands  
 E-mail: m.tsampas@diffier.nl

A. Ranade, A. Ranade  
 Inorganic Membranes and Membrane Reactors  
 Sustainable Process Engineering  
 Department of Chemical Engineering and Chemistry  
 Eindhoven University of Technology  
 De Rondom 70, Eindhoven 5612 AP, The Netherlands

 The ORCID identification number(s) for the author(s) of this article can be found under <https://doi.org/10.1002/admi.202300486>

© 2023 The Authors. Advanced Materials Interfaces published by Wiley-VCH GmbH. This is an open access article under the terms of the Creative Commons Attribution License, which permits use, distribution and reproduction in any medium, provided the original work is properly cited.

DOI: 10.1002/admi.202300486

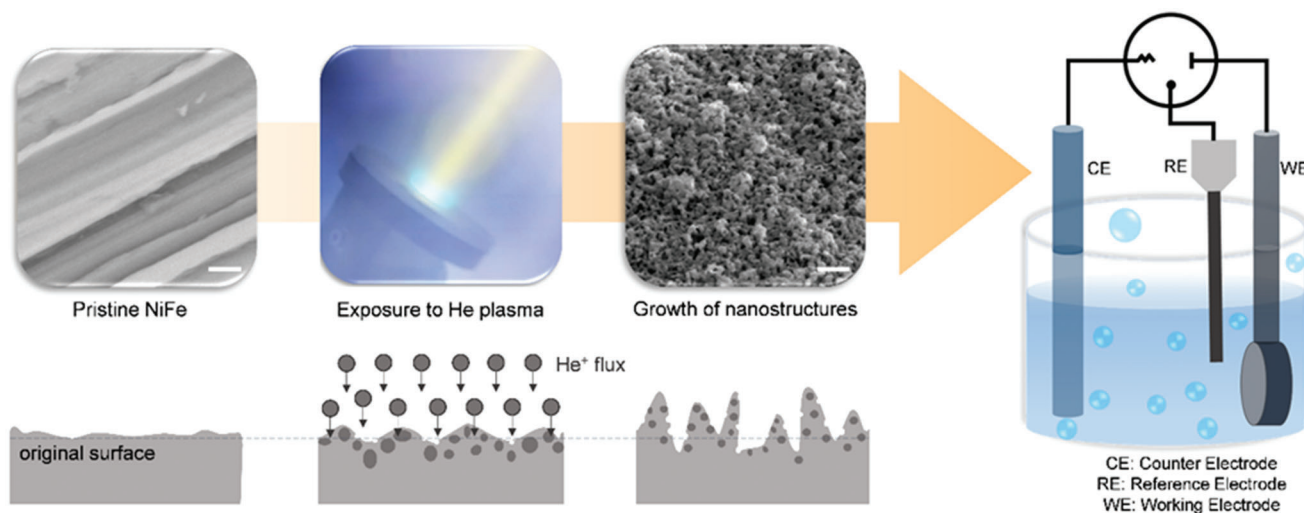


**Figure 1.** Schematic illustration of the growth of nanostructures on metallic surfaces. The self-supported nanostructures are utilized as electrocatalysts for water electrolysis in alkaline media. Scale bar: 500 nm.

bonding strength.<sup>[34,35]</sup> These factors reduce the electrochemical performance and limit the applicability of conventional nanostructured electrocatalysts on a practical scale. This implies that there is a need of exploring novel nanostructuring approaches in order to expand the library of the electrocatalyst fabrication methods.

Helium plasma irradiation (consisting of a high flux of low energy ions) is a potential alternative wherein the nanostructures are grown on the substrate itself. Commonly termed as “fuzz”, the nanostructures grown via plasma irradiation were first observed on a tungsten surface while studying the plasma-wall interactions of a fusion reactor.<sup>[36]</sup> The growth of fuzz can modify the rate of surface erosion that causes embrittlement of the divertor, ultimately affecting the reactor performance. Since its discovery, there have been multiple experimental, theoretical and numerical studies to model the fuzz growth and identify the underlying mechanisms.<sup>[37,38]</sup> In this direction, plasma nanostructuring has been realized on titanium, nickel, iron, tantalum, molybdenum<sup>[39–41]</sup> as well as on precious metals such as ruthenium, iridium, platinum.<sup>[42]</sup>

Apart from fusion research, a few studies have investigated this technique in the field of photoelectrochemical hydrogen production, wherein nanostructuring of photo-absorbers was achieved for improving the performance.<sup>[41,43,44]</sup> Additionally, other plasma species (such as O<sub>2</sub>, H<sub>2</sub>, N<sub>2</sub>, and PH<sub>3</sub>) have been utilized to enhance the chemical structure and/or morphology of the electrocatalyst.<sup>[45–48]</sup> These studies typically utilized low-energy plasmas for modifying catalyst coatings, and the plasma-induced modifications are mainly focused on the near-surface region. The reactivity of the plasma species employed induced chemical changes like oxidation, reduction, and introduction of phosphorus or nitrogen into the surface of the catalysts. On the contrary, He plasma does not affect the material composition (due to inert nature of He), and has bulk effects as compared to the previous techniques. As a result, this technique becomes suitable for nanostructuring substrates. To the best of our knowledge, helium plasma nanostructuring in the field of water elec-

trolysis has not been investigated yet. As Ni-based materials are promising low-cost alternatives for water electrolysis, nanostructuring by helium plasma and its effect on the electrochemical performance represents a useful case study. Moreover, using helium plasma can overcome the two main bottlenecks of fabricating nanostructured electrodes: i) Influence of heterogeneous substrates by fabricating self-supported nanostructures, and ii) Zero-chemical waste while maintaining the intrinsic material properties.<sup>[49]</sup>

Hence, to incorporate plasma irradiation as a sustainable electrocatalyst fabrication method, we have developed nanostructures on NiFe foils by helium plasma irradiation and evaluated their electrochemical performance in alkaline media (schematically represented in **Figure 1**). The morphology, physical composition and the thickness of nanostructures are analyzed by various spectroscopic techniques and the electrochemical characterization compares the performance of the nanostructures to the planar unmodified surfaces. This work aims to pave the way for exploiting helium plasma irradiation for the development of nanostructured electrocatalysts based on low-cost, earth-abundant materials.

## 2. Results and Discussion

### 2.1. Structural Analysis

The morphology of the Ni-based surfaces is modified after exposure to a high flux of low-energy helium ions. Various studies have attempted to understand the mechanism of fuzz formation and the broad consensus has attributed it to the formation and coalescence of helium bubbles in the near-surface region, that after bursting create fuzz.<sup>[50]</sup> During plasma irradiation, individual He atoms diffuse through the surface and form helium clusters. The clusters then eject the host metal (in this case, NiFe), forming a Frenkel pair and subsequently reorganizing the interstitial atoms. This results in clustering of interstitials into prismatic dislocation loops. As more He atoms cluster

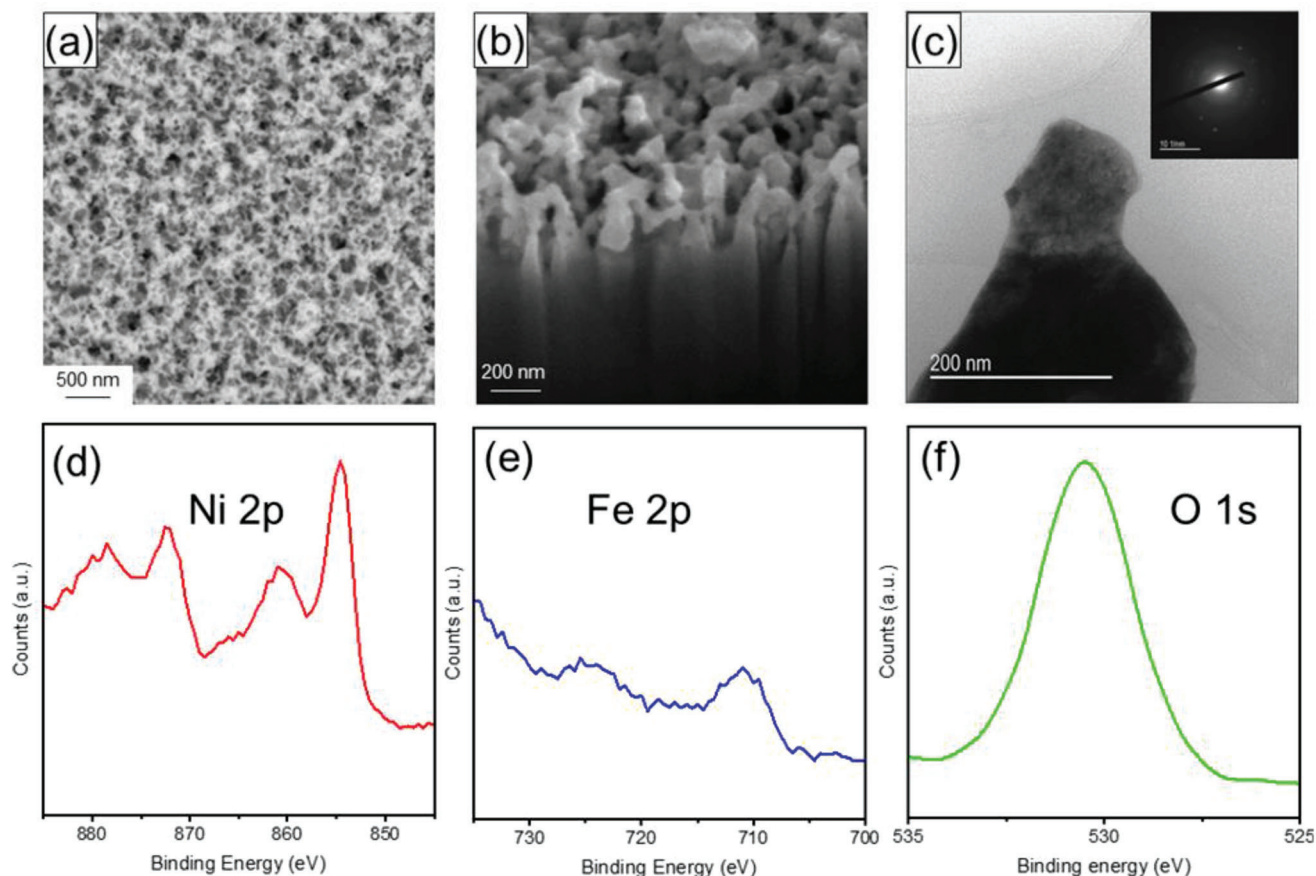


**Figure 2.** a) SEM image of NiFe nanostructures, b) cross-sectional view of nanostructures, c) TEM image of nanostructures attached to the metallic substrate (inset: SAED pattern from the region shown in (c)), d–f) XPS spectra of Ni 2p, Fe 2p, and O 1s regions.

together, the size and/or pressure of loops (commonly called He bubbles) increases, whereby it effectively bursts, leaving nano-tendrils attached to the surface.<sup>[51,52]</sup> This way, the nanostructures are grown on the surface.

The morphology of the NiFe nanostructures, as observed from SEM (Figure 2a) exhibits a fuzz-like growth with a thickness of  $\approx 200$  nm (Figure 2b). The EDS mapping of the elements (Figure S1a–d, Supporting Information) indicate that Ni, Fe and O are uniformly distributed throughout the sample. Additionally, the proportion of nickel and iron in different regions is comparable to that of the pristine alloy. This suggests that the original chemical composition of the sample does not change significantly after plasma irradiation. Figure 2c displays a TEM image, wherein the nano-tendrils attached to the metallic substrate are visible. On the surface, a thin layer ( $\approx 10$  nm) is observed, presumably corresponding to the oxidized portion and adventitious hydrocarbons. The selected area diffraction pattern (SAED) confirms the existence of metallic species and a weak marginal signal from the oxide. The XRD patterns of the NiFe nanostructures is shown in Figure S1e (Supporting Information), where the main peaks correspond to the metal substrate, suggesting that the fuzz grown is either locally ordered and/or the oxides too thin, all of which cannot be detected by the XRD.

XPS analysis was performed to obtain information about the electronic states and the elemental composition of the surface re-

gion of the samples, shown in Figure 2d–f. In the Ni 2p spectra, the Ni  $2p_{3/2}$  peak at 856 eV and the Ni  $2p_{1/2}$  peak at 873 eV can be ascribed to Ni(II) species. The broad peaks centering  $\approx 862$  and 880 eV are related to the shakeup satellites. The Fe 2p spectra displays two broad peaks  $\approx 712$  and 725 eV, with a small satellite peak  $\approx 719$  eV, indicating that the Fe is predominantly in 2+ and/or 3+ state. Regarding the O1s spectra, the main peak centering  $\approx 531$  eV can be ascribed to the hydroxide species on the surface. These results corroborate that the nanostructures have a thin layer of oxides (detected by XPS) while the bulk is present in the metallic state (detected by XRD, SAED). The physical characterization of nickel nanostructures fabricated via plasma irradiation is given in Figure S2 (Supporting Information). Additionally, the morphology of the Ni and NiFe samples before the plasma exposure, that is, before nanostructuring is shown in Figure S3 (Supporting Information).

## 2.2. Electrochemical Performance

The morphological changes that take place via plasma irradiation increase the surface area available for reactions. Hence, it is necessary to compare the active sites of nanostructures with those of planar electrodes. Although various techniques can be used to determine the active surface area of Ni-based catalysts,<sup>[53]</sup> most

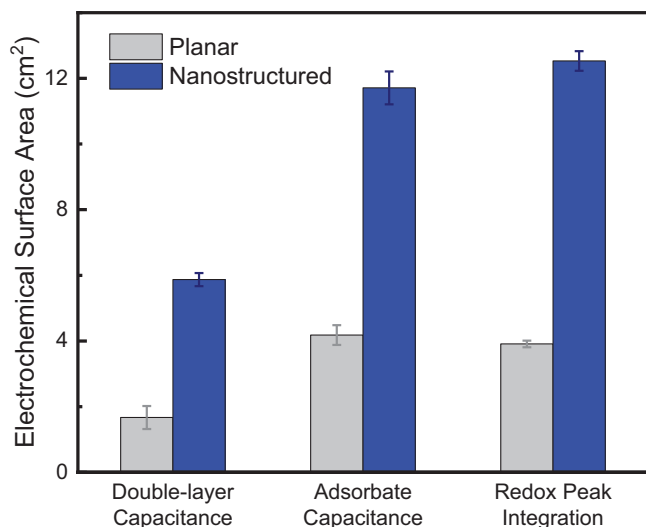


**Figure 3.** Comparison of electrochemical surface area of NiFe/n and NiFe/p by double-layer capacitance, adsorbate capacitance and redox-peak integration methods.

conventional methods possess certain inherent limitations such as low conductivity of Ni(II) compounds,<sup>[54]</sup> influence of trapped oxidized films during Ni(II)  $\rightleftharpoons$  Ni(III) transition,<sup>[55]</sup> structural evolution,<sup>[56]</sup> electrochemical conditioning,<sup>[57]</sup> all of which limit accurate active area measurements. In addition, the complexity of Ni-based electrochemistry also calls for assumptions and estimations when trying to measure the active surface area. Thus, to get a better representative scenario, the active sites of nanostructures and planar surfaces are compared using double-layer capacitance, adsorbate capacitance, and redox peak integration methods (Figure 3). It is observed that irrespective of the method employed, approximately a 3 to 4 times increase in the active surface area is observed for nanostructures as compared to planar electrodes. Thus, even under various assumptions, the increased active sites via nanostructuring can be primarily attributed to the improvement in the electrochemical performance.

The OER performance of the NiFe nanostructures (NiFe/n) and other control samples was evaluated in a 1 M KOH solution. As shown in Figure 4a, synergistic effects between nickel and iron achieve a high electrochemical performance, wherein NiFe nanostructures (NiFe/n) achieve  $\approx 2.5$  times higher current density than planar NiFe foils (NiFe/p) at 1.7 V. The redox peak centering  $\approx 1.4$  V is associated with the Ni<sup>2+/3+</sup> transformation. Iron incorporation shifts this peak anodically, and this phenomena has been well documented in literature.<sup>[58,59]</sup> The benchmark  $10 \text{ mA cm}^{-2}_{\text{geo}}$  current density is achieved at 330 mV for NiFe/n, and 378 mV for NiFe/p, comparable with other state-of-the-art catalysts (Table S1, Supporting Information). In comparison, nickel nanostructures (Ni/n) and planar nickel foil (Ni/p) require overpotentials of 372 and 452 mV respectively, to deliver  $10 \text{ mA cm}^{-2}_{\text{geo}}$ . For Ir, IrO<sub>x</sub> nanoparticles are typically deposited on a heterogeneous substrate when employed as electrocatalysts. However, in order to have similar catalyst design, an Ir/IrO<sub>x</sub> foil was used for comparison. In this case the overpotential to reach  $10 \text{ mA cm}^{-2}_{\text{geo}}$  is 426 mV, which is in good agreement with literature.<sup>[1]</sup> The polarization curves for OER (Figure 4a) are also

normalized by the ECSA in Figure S4a (Supporting Information) (via adsorbate capacitance method). The Tafel plots (Figure 4b) provide further insights into the kinetics of electrocatalysts. The NiFe/n has the lowest Tafel slope, suggesting fast reaction kinetics for OER. This is consistent with the EIS (Figure S5a, Supporting Information), wherein lower charge transfer resistance suggests higher conductivity and a faster charge transfer process. The faradaic efficiency of 97% for oxygen production measured at a constant current density of  $10 \text{ mA cm}^{-2}_{\text{geo}}$  (Figure 4c) suggests that almost all charge is utilized for OER, without any parasitic reactions.

Long-term durability tests were performed to evaluate the stability of the nanostructured catalysts (Figure 4d). At a constant current density of  $10 \text{ mA cm}^{-2}_{\text{geo}}$ , the NiFe/n shows excellent stability, degrading only by  $\approx 30$  mV in 100 h. In comparison, Ni/n degrade  $\approx 100$  mV in 100 h. Post the durability test, the morphology of the nanostructures is observed via SEM (Figure S6a, Supporting Information). The depth of the nanostructures (Figure S6c, Supporting Information) remains the same ( $\approx 200$  nm), indicating that even after long-term testing ( $>100$  h), no mechanical shedding or weakening of the nano-tendrils is observed. The XRD patterns of the reacted nanostructures exhibit metallic peaks (Figure S6d, Supporting Information), and the XPS spectra (Figure S7a–c, Supporting Information) indicate complete oxidation of the surface. These results indicate the robustness of the electrocatalysts and their applicability on a practical level.

The HER performance of the NiFe nanostructures (NiFe/n) and other control samples was also tested in 1 M KOH solution. As shown in Figure 5a, Ni/p requires an overpotential of 450 mV, while NiFe/p requiring 384 mV to achieve  $10 \text{ mA cm}^{-2}_{\text{geo}}$ . Nanostructuring increases the number of active sites, thus alleviating the overpotentials to 319 mV for Ni/n and 354 mV for NiFe/n, to deliver  $10 \text{ mA cm}^{-2}_{\text{geo}}$  (this is comparable with literature data presented in Table S2, Supporting Information). Pt foil shows superior HER activity with an overpotential of 196 mV to achieve  $10 \text{ mA cm}^{-2}_{\text{geo}}$ . The polarization curves for HER (Figure 5a) are also normalized by the ECSA in Figure S4b (Supporting Information). Comparing the Tafel slopes from Figure 5b, both Ni/p and Ni/n exhibit similar Tafel slopes suggesting similar mechanisms for HER. This is also observed in EIS (Figure S5b, Supporting Information), wherein the charge transfer resistance of the planar as well as nanostructured samples is comparable. In case of NiFe samples, similar trend is observed, albeit at lower Tafel slopes. The NiFe/n exhibits a faradaic efficiency of 96% (Figure 5c) for hydrogen production, which suggests that almost all charge is utilized for HER, and not for other parasitic reactions.

When considering the stability of electrodes for HER, monometallic nickel exhibits suboptimal results. At a constant current density of  $10 \text{ mA cm}^{-2}_{\text{geo}}$ , the Ni/n degrades  $>300$  mV in 100 h. This is primarily caused by hydride formation, which increases the hydrogen concentration on the surface and thus requires additional potential to carry the reaction.<sup>[60]</sup> Incorporation of iron mitigates hydride formation and helps to improve the long-term stability. This is duly observed for NiFe/n, which shows a smaller increase in potential ( $\approx 70$  mV) during 100 h of chronopotentiometry (Figure 5d). The physical morphology of NiFe/n post the durability test is shown in Figure S6b (Supporting Information), wherein the nanostructures are observed on the surface. The XPS spectra (Figure S7d–f, Supporting Information) show nickel and

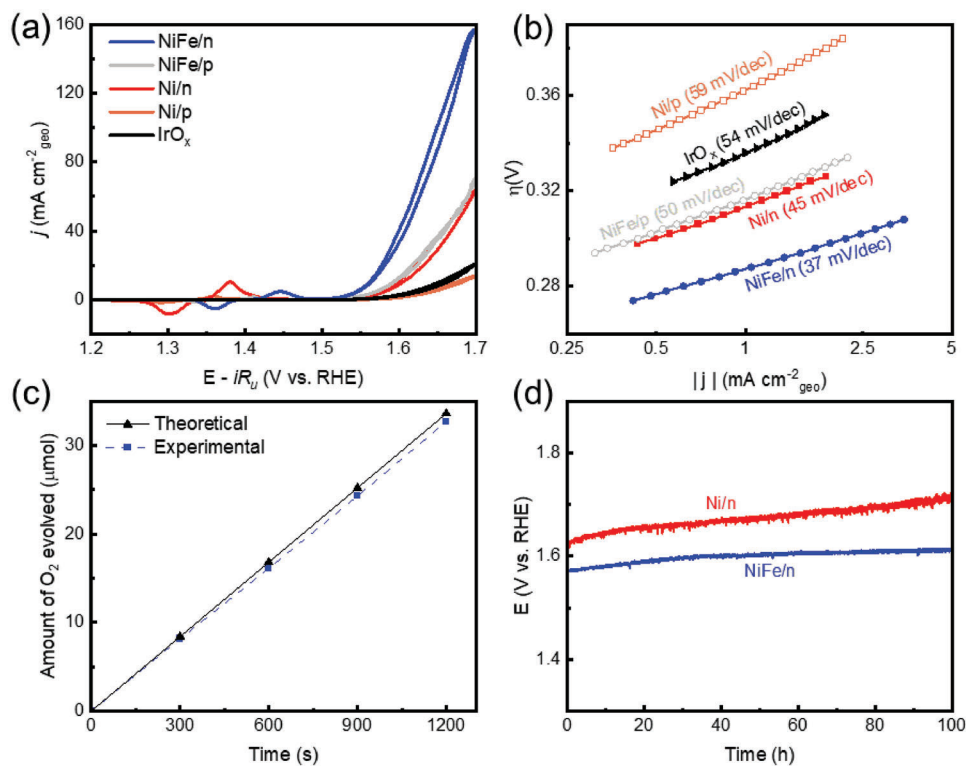


**Figure 4.** a) LSV polarization curves for OER at 20 mVs<sup>-1</sup> after the accelerated durability test, b) Tafel slopes for OER, c) Faradaic efficiency measurement for OER at 10 mA cm<sup>-2</sup><sub>geo</sub>, and d) stability measurement of Ni/n and NiFe/n for 100 h at 10 mA cm<sup>-2</sup><sub>geo</sub>.

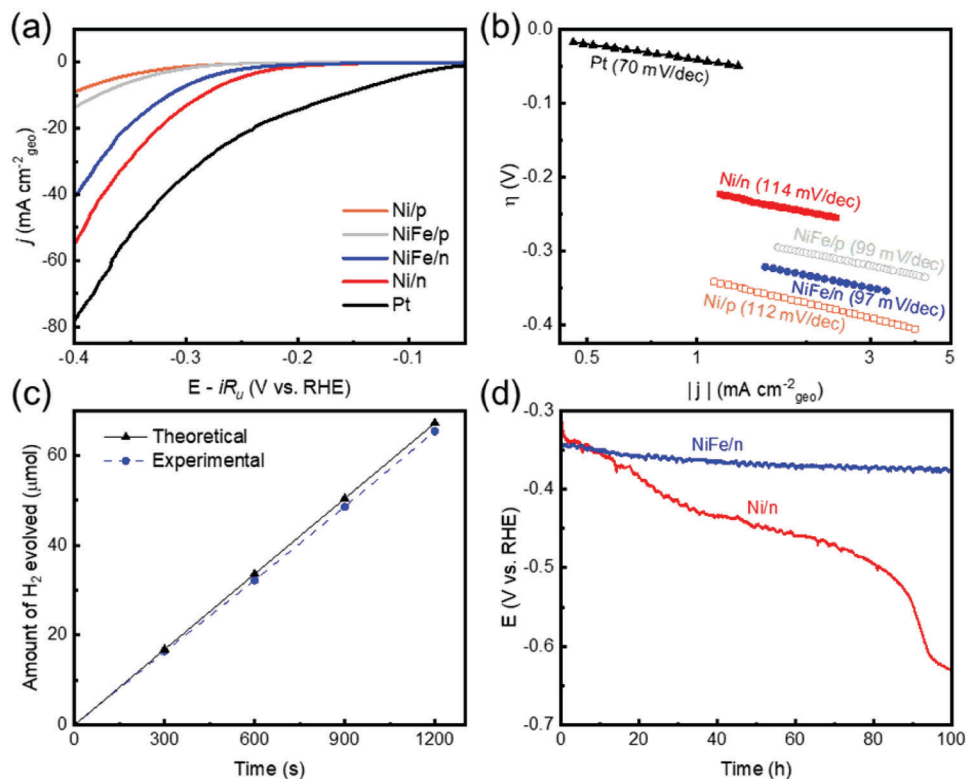


**Figure 5.** a) LSV polarization curves for HER at 20 mVs<sup>-1</sup> after the accelerated durability test, b) Tafel slopes for HER, c) Faradaic efficiency measurement for HER at 10 mA cm<sup>-2</sup><sub>geo</sub>, and d) stability measurement of Ni/n and NiFe/n for 100 h at 10 mA cm<sup>-2</sup><sub>geo</sub>.

iron predominantly in their oxidized states (presumably due to OH<sup>-</sup> adsorption and/or dissolved oxygen). This is also corroborated from the O 1s spectra where the main peak corresponds to the hydroxide species on the surface of the catalyst.

The bifunctional activity and stability of the nanostructured electrodes were also tested in a two-electrode configuration, and is shown in Figure S8 (Supporting Information). The benchmark 10 mAcm<sup>-2</sup><sub>geo</sub> current density is achieved at 1.81 V for Ni/n and 1.91 V for NiFe/n. However, the NiFe/n catalyst shows superior stability (≈50 mV decay) as compared to Ni/n which shows ≈300 mV decay during 100 h of chronopotentiometric testing.

The current results were focused only on planar substrates to demonstrate the applicability of this technique as an electrocatalyst fabrication method, and to showcase the advantages of fabricating self-supported nanostructured-electrodes via helium plasma irradiation. As a next step, achieving plasma nanostructuring of 3D substrates (e.g., felts, foams, mesh) can find practical applications in various sustainable systems such as water electrolyzers, fuel cells, super-capacitors, and batteries.

### 3. Conclusion

In summary, helium plasma irradiation was employed for nanostructuring nickel-based planar substrates, which were evaluated for the first time for water electrolysis in alkaline media. The top-down approach of developing nanostructures does not generate chemical waste and can have a zero-carbon footprint when coupled with renewable energy sources. In addition, the growth of self-supported nanostructures overcomes the issues related to the adherence of the active materials on the electrode support or blocking of active sites, which is often the case in conventional methods. In essence, the nanostructures fabricated via plasma irradiation had an electrochemical surface area 3 to 4 times higher than the unmodified planar substrates. This improved the electrocatalytic activity for OER and HER by approximately three times, as compared to the planar surfaces. Going forward, the versatile nature of plasma technology and the desirable characteristics of mixed-metal oxides can be further integrated to advance and find practical applications in next-generation renewable energy systems.

### 4. Experimental Section

**Material Synthesis:** NiFe (Ni:Fe = 4:1) foils (1 mm thickness, Goodfellow, 99.99 wt.%) were ultrasonicated with acetone, ethanol, and deionized water for 20 min each prior to use. Nanostructuring on the metal surfaces was obtained by exposing the foils to helium plasma in a linear plasma generator (Upgraded Pilot-PSI).<sup>[61]</sup> Here, the plasma was generated by a cascaded arc source that exhausts into a vacuum vessel. An axial magnetic field was used to confine the plasma and generate a magnetized cylindrical plasma beam. The nanostructures were formed by exposing the surface to helium ions with incident energy up to 70 eV and a flux of 6–7 × 10<sup>23</sup> m<sup>-2</sup>s<sup>-1</sup> at a surface temperature of ≈923 K (650 °C) for a duration of 300 s. To remove any possible impurities or contamination from the plasma device, the foils were washed with deionized water after nanostructuring. The plasma conditions were selected based on the relevant literature<sup>[62]</sup> as the scope of this work was mainly to investigate the electrochemical performance of nanostructured substrates due to plasma irradiation.

**Material Characterization:** Scanning electron microscopy with the backscattered electron detector (SEM; Desktop Phenom-Pharos, Thermo

Fisher Scientific) and transmission electron microscope (TEM; JEOL JEM-2100) were used to examine the morphology of the nanostructured electrocatalysts. A dual beam scanning electron microscope (SEM/FIB; FEI nova6001 Nanolab) using the secondary electron detector to image the cross-section of the surface after focused ion beam erosion, was used to measure the thickness and the uniformity of the nanostructured electrocatalysts. Energy-dispersive X-ray spectroscopy (EDS; Phenom-Pharos, Thermo Fisher Scientific) was performed to determine the elemental composition of the electrocatalysts. X-ray Diffractometry (XRD; Bruker D8 eco) using Cu K<sub>α</sub> was used to determine the crystallinity of the electrocatalysts. To increase surface sensitivity, fixed grazing angle XRD was employed at 1°, limiting the information depth to ≈1 μm for Ni or NiFe. The surface chemical analysis was carried out by X-ray Photoelectron Spectroscopy (XPS) was performed with a Mg K<sub>α</sub> non-monochromatic source (VG CLAMP1) at 75 eV constant pass energy. The Binding energy (BE) scale of the spectra was referenced to the C 1s line of the adventitious carbon contamination at 284.8 eV.

**Electrochemical Measurements:** The electrochemical measurements were carried out in a three-electrode cell using an Ivium-n-stat 1A.EIS (Ivium Technologies B.V., the Netherlands). 1 M KOH (VWR) was used as the electrolyte for all experiments. NiFe foils (1 cm<sup>2</sup> geometric area exposed to electrolyte), graphite rod (redox.me), and a Gaskatel Hydroflex RHE (Gaskatel GmbH, Germany) were used as the working electrode, counter electrode, and the reference electrode respectively. A Platinum and an Iridium foil (Alfa Aesar, 99.9%) were used as benchmark catalysts for comparison. Ir foil was converted to IrO<sub>x</sub> as described in the Supporting Information.

The electrochemical analysis was performed in the following protocol: Electrochemical Impedance Spectroscopy (EIS) measurements were performed at open-circuit conditions in a frequency range from 100 kHz to 0.1 Hz and an amplitude of 10 mV. All electrochemical results are compensated with 80% solution resistance (obtained from EIS). The electrode performance was tested by accelerated durability test via cyclic voltammetry (CV) scans for 1000 cycles at a scan rate of 50 mV s<sup>-1</sup>. The applied potential window was from 1.2 to 1.7 V for OER and -0.05 to -0.4 V for HER. The Tafel slope and the overpotential were determined by linear sweep voltammetry (LSV; scan rate 1 mV s<sup>-1</sup>). Chronopotentiometric transient experiments at 10 mA cm<sup>-2</sup><sub>geo</sub> for 100 h were performed to test the stability of the electrodes. The faradaic efficiency was calculated by comparing the theoretical gases produced to the actual gases produced, and further details are given in the Supporting Information. The electrochemical surface area was determined by double-layer capacitance, adsorbate capacitance and redox-peak integration methods, and further details are described in Figures S9–S11 (Supporting Information). The two-electrode performance was determined by LSV from 1.2 to 2 V at 5 mV s<sup>-1</sup> and the stability test was carried out at 10 mAcm<sup>-2</sup><sub>geo</sub> for 100 h.

### Supporting Information

Supporting Information is available from the Wiley Online Library or from the author.

### Acknowledgements

This work has been carried out within the ECCM SCALE Project (no. NWA.1237.18.001) funded jointly by the Dutch Organization for Scientific Research. The authors would like to thank the co-funders of the project ISPT, Syngaschem, VecoPrecision and Vsparticle and international partners Toyota Motor Europe and FORTH institute. The authors thank Jordy Vernimmen for performing the Thomson scattering measurements. The authors also thank Richard Al and Marc van der Pol for their insights during plasma experiments in UPP.

### Conflict of Interest

The authors declare no conflict of interest.

## Data Availability Statement

The data that support the findings of this study are openly available in Zenodo at <https://doi.org/10.5281/zenodo.8028371>, reference number 54.

## Keywords

helium plasma, NiFe-based electrocatalysts, plasma nanostructuring, water splitting

Received: June 12, 2023

Revised: August 11, 2023

Published online: September 4, 2023

- [1] C. C. L. McCrory, S. Jung, I. M. Ferrer, S. M. Chatman, J. C. Peters, T. F. Jaramillo, *J. Am. Chem. Soc.* **2015**, *137*, 4347.
- [2] H. J. Kim, H. Y. Kim, J. Joo, S. H. Joo, J. S. Lim, J. Lee, H. Huang, M. Shao, J. Hu, J. Y. Kim, B. J. Min, S. W. Lee, M. Kang, K. Lee, S. Choi, Y. Park, Y. Wang, J. Li, Z. Zhang, J. Ma, S.-I. Choi, *J. Mater. Chem. A* **2022**, *10*, 50.
- [3] F. M. Sapountzi, E. D. Orlova, J. P. S. Sousa, L. M. Salonen, O. I. Lebedev, G. Zafeiropoulos, M. N. Tsampas, H. J. W. Niemantsverdriet, Y. V. Kolen'ko, *Energy Fuels* **2020**, *34*, 6423.
- [4] W. Zhang, D. Li, L. Zhang, X. She, D. Yang, *J. Energy Chem.* **2019**, *39*, 39.
- [5] J. Z. Soo, B. Gupta, A. Riaz, C. Jagadish, H. H. Tan, S. Karuturi, *Chem. Mater.* **2022**, *34*, 6792.
- [6] F. Wu, X. Guo, G. Hao, Y. Hu, W. Jiang, *Adv. Mater. Interfaces* **2019**, *6*, 1900788.
- [7] Y. Sun, S. Xu, C. A. Ortíz-Ledón, J. Zhu, S. Chen, J. Duan, C. J. Zhu, *Exploration* **2021**, *1*, 20210021.
- [8] X. Yan, Y. Zou, Y. Zhang, *Mater. Future* **2023**, *2*, 022102.
- [9] M. Gong, D. Y. Wang, C. C. Chen, B. J. Hwang, H. Dai, *Nano Res.* **2015**, *9*, 28.
- [10] V. Vij, S. Sultan, A. M. Harzandi, A. Meena, J. N. Tiwari, W.-G. Lee, T. Yoon, K. S. Kim, *ACS Catal.* **2017**, *7*, 7196.
- [11] E. López-Fernández, C. G. Sacedón, J. Gil-Rostra, F. Yubero, A. R. González-Elipe, A. de Lucas-Consuegra, *Molecules* **2021**, *26*, 6326.
- [12] N. Plankensteiner, A. Agosti, J. Govaerts, R. Rupp, S. Singh, J. Poortmans, P. M. Vereecken, J. John, *Sol. RRL* **2023**, *7*, 2201095.
- [13] L. Trotochaud, S. L. Young, J. K. Ranney, S. W. Boettcher, *J. Am. Chem. Soc.* **2014**, *136*, 6744.
- [14] S. Klaus, Y. Cai, M. W. Louie, L. Trotochaud, A. T. Bell, *J. Phys. Chem. C* **2015**, *119*, 7243.
- [15] D. M. Soares, O. Teschke, I. Torriani, *J. Electrochem. Soc.* **1992**, *139*, 98.
- [16] A. E. Mauer, D. W. Kirk, S. J. Thorpe, *Electrochim. Acta* **2007**, *52*, 3505.
- [17] N. Danilovic, R. Subbaraman, D. Strmcnik, K.-C. Chang, A. P. Paulikas, V. R. Stamenkovic, N. M. Markovic, *Angew. Chem., Int. Ed.* **2012**, *51*, 12495.
- [18] T. Zhan, Y. Zhang, X. Liu, S. Lu, W. Hou, *J. Power Sources* **2016**, *333*, 53.
- [19] Y. Jia, L. Zhang, G. Gao, H. Chen, B. Wang, J. Zhou, M. T. Soo, M. Hong, X. Yan, G. Qian, J. Zou, A. Du, X. Yao, *Adv. Mater.* **2017**, *29*, 1700017.
- [20] A. Kumar, S. Bhattacharyya, *ACS Appl. Mater. Interfaces* **2017**, *9*, 41906.
- [21] H. Zhang, X. Li, A. Hähnel, V. Naumann, C. Lin, S. Azimi, S. L. Schweizer, A. W. Maijenburg, R. B. Wehrspohn, *Adv. Funct. Mater.* **2018**, *28*, 1706847.
- [22] Z. Chen, X. Liu, T. Shen, C. Wu, L. Zu, L. Zhang, *Int. J. Hydrogen Energy* **2021**, *46*, 37736.
- [23] Z. W. Seh, J. Kibsgaard, C. F. Dickens, I. Chorkendorff, J. K. Nørskov, T. F. Jaramillo, *Science* **2017**, *355*, <https://doi.org/10.1126/science.aad4998>.
- [24] J. Siddiqui, T. Hussain, R. S. Rawat, *J. Phys.: Conf. Ser.* **2015**, *591*, 012021.
- [25] X. Li, X. Hao, A. Abudula, G. Guan, *J. Mater. Chem. A* **2016**, *4*, 11973.
- [26] M. Gao, W. Sheng, Z. Zhuang, Q. Fang, S. Gu, J. Jiang, Y. Yan, *J. Am. Chem. Soc.* **2014**, *136*, 7077.
- [27] G. Liu, K. Wang, X. Gao, D. He, J. Li, *Electrochim. Acta* **2016**, *211*, 871.
- [28] F. Ganci, T. Baguet, G. Aiello, V. Cusumano, P. Mandin, C. Sunseri, R. Inguanta, *Energies* **2019**, *12*, 3669.
- [29] E. López-Fernández, J. Gil-Rostra, J. P. Espinós, A. R. González-Elipe, A. de Lucas Consuegra, F. Yubero, *ACS Catal.* **2020**, *10*, 6159.
- [30] C. Sun, Q. Song, J. Lei, D. Li, L. Li, F. Pan, *ACS Appl. Energy Mater.* **2021**, *4*, 8791.
- [31] E. Cossar, K. Agarwal, V. B. Nguyen, R. Safari, G. A. Botton, E. A. Baranova, *Electrocatalysis* **2021**, *12*, 605.
- [32] N. Plankensteiner, R. Rupp, P. Steegstra, S. Singh, J. G. Canto, S. Wodarz, M. J. W. Blom, J. John, M. Mees, P. M. Vereecken, *Mater. Today Energy* **2022**, *30*, 101172.
- [33] J. E. Park, S. Park, M.-J. Kim, H. Shin, S. Y. Kang, Y.-H. Cho, Y.-E. Sung, *ACS Catal.* **2022**, *12*, 135.
- [34] C. Wei, R. R. Rao, J. Peng, B. Huang, I. E. L. Stephens, M. Risch, Z. J. Xu, Y. Shao-Horn, *Adv. Mater.* **2019**, *31*, 1806296.
- [35] E. López-Fernández, C. Gómez-Sacedón, J. Gil-Rostra, J. P. Espinós, A. R. González-Elipe, F. Yubero, A. de Lucas-Consuegra, *Chem. Eng. J.* **2022**, *433*, 133774.
- [36] S. Takamura, N. Ohno, D. Nishijima, S. Kajita, *Plasma Fusion Res.* **2006**, *1*, 051.
- [37] S. Takamura, Y. Uesugi, *Appl. Surf. Sci.* **2015**, *356*, 888.
- [38] A. M. Ito, A. Takayama, Y. Oda, T. Tamura, R. Kobayashi, T. Hattori, S. Ogata, N. Ohno, S. Kajita, M. Yajima, Y. Noiri, Y. Yoshimoto, S. Saito, S. Takamura, T. Murashima, M. Miyamoto, H. Nakamura, *J. Nucl. Mater.* **2015**, *463*, 109.
- [39] G. De Temmerman, K. Bystrov, J. J. Zielinski, M. Balden, G. Matern, C. Arnas, L. Marot, *J. Vac. Sci. Technol., A* **2012**, *30*, 041306.
- [40] S. Kajita, T. Ishida, N. Ohno, D. Hwangbo, T. Yoshida, *Sci. Rep.* **2016**, *6*, 30380.
- [41] A. Bieberle-Hütter, I. Tanyeli, R. Lavrijsen, B. Koopmans, R. Sinha, M. C. M. van de Sanden, *Thin Solid Films* **2017**, *631*, 50.
- [42] S. Kajita, T. Nojima, Y. Tomita, N. Ohno, H. Tanaka, N. Yoshida, M. Yajima, T. Akiyama, M. Tokitani, T. Yagi, *Surf. Coat. Technol.* **2018**, *340*, 86.
- [43] M. de Respinis, G. De Temmerman, I. Tanyeli, M. C. M. van de Sanden, R. P. Doerner, M. J. Baldwin, R. van de Krol, *ACS Appl. Mater. Interfaces* **2013**, *5*, 7621.
- [44] S. Feng, S. Kajita, M. Higashi, A. Bieberle-Hütter, T. Yoshida, N. Ohno, *Appl. Surf. Sci.* **2022**, *580*, 151979.
- [45] H. Liang, A. N. Gandhi, D. H. Anjum, X. Wang, U. Schwingenschlög, H. N. Alshareef, *Nano Lett.* **2016**, *16*, 7718.
- [46] H. Liang, A. N. Gandhi, C. Xia, M. N. Hedhili, D. H. Anjum, U. Schwingenschlög, H. N. Alshareef, *ACS Energy Lett.* **2017**, *2*, 1035.
- [47] Y. Tang, Q. Liu, L. Dong, H. Bin Wu, X.-Y. Yu, *Appl. Catal., B* **2020**, *266*, 118627.
- [48] V. Kyriakou, R. K. Sharma, D. Neagu, F. Peeters, O. De Luca, P. Rudolf, A. Pandiyan, W. Yu, S. W. Cha, S. Welzel, M. C. M. van de Sanden, M. N. Tsampas, *Small Methods* **2021**, *5*, 2100868.
- [49] S. Dou, L. Tao, R. Wang, S. El Hankari, R. Chen, S. Wang, S. Dou, L. Tao, R. Wang, S. E. Hankari, R. Chen, S. Wang, *Adv. Mater.* **2018**, *30*, 1705850.
- [50] S. Kajita, A. M. Ito, K. Imano, *J. Appl. Phys.* **2022**, *132*, 181101.
- [51] F. Sefta, K. D. Hammond, N. Juslin, B. D. Wirth, *Nucl. Fusion* **2013**, *53*, 073015.
- [52] D. Dasgupta, R. D. Kolasinski, R. W. Friddle, L. Du, D. Maroudas, B. D. Wirth, *Nucl. Fusion* **2019**, *59*, 086057.



- [53] E. Cossar, M. S. E. Houache, Z. Zhang, E. A. Baranova, *J. Electroanal. Chem.* **2020**, *870*, 114246.
- [54] S. S. Jeon, P. W. Kang, M. Klingenhof, H. Lee, F. Dionigi, P. Strasser, *ACS Catal.* **2023**, *13*, 1186.
- [55] A. S. Batchellor, S. W. Boettcher, *ACS Catal.* **2015**, *5*, 6680.
- [56] C. Dette, M. R. Hurst, J. Deng, M. R. Nellist, S. W. Boettcher, *ACS Appl. Mater. Interfaces* **2019**, *11*, 5590.
- [57] Y. J. Son, S. Kim, V. Leung, K. Kawashima, J. Noh, K. Kim, R. A. Marquez, O. A. Carrasco-Jaim, L. A. Smith, H. Celio, D. J. Milliron, B. A. Korgel, C. B. Mullins, *ACS Catal.* **2022**, *12*, 10384.
- [58] D. A. Corrigan, *J. Electrochem. Soc.* **1987**, *134*, 377.
- [59] M. B. Stevens, C. D. M. Trang, L. J. Enman, J. Deng, S. W. Boettcher, *J. Am. Chem. Soc.* **2017**, *139*, 11361.
- [60] S. I. Perez Bakovic, P. Acharya, M. Watkins, H. Thornton, S. Hou, L. F. Greenlee, *J. Catal.* **2021**, *394*, 104.
- [61] “Upgraded Pilot-PSI (UPP) | Dutch Institute for Fundamental Energy Research,” can be found under <https://www.differ.nl/facilities/upgraded-pilot-psi>.
- [62] S. Kajita, T. Yoshida, D. Kitaoka, R. Etoh, M. Yajima, N. Ohno, H. Yoshida, N. Yoshida, Y. Terao, *J. Appl. Phys.* **2013**, *113*, 134301.